Available online at www.sciencedirect.com
SCIENCE DIRECT
Journal of Photochemistry and Photobiology A: Chemistry 172 (2005) 35–46
Journal of Photochemistry and Photobiology A:Chemistry
www.elsevier.com/locate/jphotochem

High-resolution absorption cross-section of glyoxal in the UV–vis and IR spectral ranges

Rainer Volkamer[a,*], Peter Spietz[b], John Burrows[b], Ulrich Platt[a]

[a] *Institut für Umweltphysik, Universität Heidelberg, INF 229, 69120 Heidelberg, Germany*
[b] *Institut für Umweltphysik, Universität Bremen, Otto Hahn Allee 1, 28359 Bremen, Germany*

Received 27 May 2004; received in revised form 9 November 2004; accepted 10 November 2004
Available online 12 January 2005

Abstract

High-resolution absorption cross-sections of glyoxal have been recorded at 296 K in the ultraviolet and visible (UV–vis: 19000–40000 cm^{-1}, 250–526 nm) and infrared (IR: 1200–8000 cm^{-1}) spectral ranges by means of a Fourier transform spectrometer (FTS). The UV–vis spectra were measured at 1 atm of N_2 bath gas. The spectral resolution of the FTS was selected to be 0.06 cm^{-1} for the richly structured $\tilde{A}\ ^1A_u - \tilde{X}\ ^1A_g$ and $\tilde{a}\ ^3A_u - \tilde{X}\ ^1A_g$ band systems, and 1 cm^{-1} for the diffuse $\tilde{B} - \tilde{X}$ transition, which was sufficient to resolve most spectral structures. In addition, low and high-resolution IR spectra (1 and 0.009 cm^{-1} spectral resolution) of glyoxal/N_2 mixtures were recorded around 2835 cm^{-1} at 0.2 mbar, 100 mbar, 300 mbar and 1 atm total pressure. UV–vis and IR spectra were recorded quasi-simultaneously by making sequential measurements of identical glyoxal mixtures in the cell, enabling the direct comparison of UV–vis and IR spectral parameters for the first time.

The high-resolution spectra have been used to simulate deviations from Lambert–Beer's law, which occur at lower resolution when spectra are not fully resolved. Special attention has been paid to reduce the uncertainty of the UV–vis spectrum, allowing for an improved determination of the atmospheric photolysis of glyoxal. Finally, the new UV–vis spectrum has been used to redetermine our previous DOAS measurements of glyoxal yields from the reactions of OH radicals with benzene, toluene and *p*-xylene. The high-resolution spectral data can be obtained from http://iup.physik.uni-bremen.de/gruppen/molspec/index.html or email request to the authors.

Keywords: Glyoxal; Absorption cross-section; Gas-phase; Ultraviolet; Infrared

1. Introduction

Glyoxal (CHOCHO), the smallest α-dicarbonyl type compound, is formed in the atmosphere during the oxidation of hydrocarbons, which are emitted by biogenic and anthropogenic sources. In particular, glyoxal is an important ring-cleavage product in the OH-radical initiated oxidation of aromatic hydrocarbons [1–4], and is also formed in the reaction of O_3 and OH-radicals with some alkenes [5–8] and unsaturated aliphatic oxygenated hydrocarbons [9,10]. Minor amounts of glyoxal have been observed in automobile tailpipe emissions [11,12]. Trace quantities of glyoxal are present in butter and food products produced by fermentation processes, such as wine, brandy, beer, yoghurt, cheese, and vinegar [13,14].

The tropospheric fate of glyoxal is similar to that of formaldehyde and is largely determined by its photolysis and reaction with OH-radicals [15,16]. Alternative removal pathways include dry and wet deposition [17], transfer to aerosols, and possibly nighttime reaction with NO_3-radicals. Photolysis of glyoxal leads to the formation of H_2, CO, HCHO and HCO radicals. Atmospheric residence time with respect to photolysis is limited during the day to a few hours [15,18]. Atmospheric measurements of glyoxal are scarce, but tropo-

* Corresponding author. Present address: Earth Atmosphere and Planetary Sciences, Massachusetts Institute of Technology, Room 54-1320, 77, Massachusetts Avenue, Cambridge, MA 02141, USA. Tel.: +1 617 2532321; fax: +1 617 2586525.
E-mail address: rainer@alum.mit.edu (R. Volkamer).

1010-6030/$ – see front matter © 2004 Elsevier B.V. All rights reserved.
doi:10.1016/j.jphotochem.2004.11.011

spheric mixing ratios have been reported to range between several 100 ppt to few ppb [19–21].

As a result of the importance of photolysis among the reaction pathways of glyoxal, an accurate knowledge of the UV–vis absorption cross-section is essential to understand and quantify the atmospheric fate of this compound. The glyoxal UV–vis spectrum has been studied in several investigations [15,22–26], and some information on band assignments is available [27–29]. Considerable uncertainty remains associated with the low cross-section values around 350 nm, which are known within only ±40%. The actinic photon flux of the sun in the troposphere compensates for the relatively low cross-section at this wavelength, and a significant portion of the tropospheric photolysis takes place at wavelengths around 350 nm and below. A better knowledge of the cross-section is therefore desirable.

Recently, differential optical absorption spectroscopy (DOAS) has been used in an extensive study of the oxidation of aromatic hydrocarbons and the uncertainty in the cross-section of glyoxal was identified as one of the limiting factors in interpretation of the observations [2,30]. Glyoxal poses several problems for its measurement by DOAS:

(1) The recording of reference spectra in the field is not straightforward, because glyoxal in a portable cuvette degrades upon exposure to measurement light, sunlight and the formation of polymers, and can induce spectral interferences from the formation of formaldehyde.
(2) The spectral calibration of existing glyoxal reference spectra is not sufficiently well known.
(3) The available low-resolution literature cross-sections limit the DOAS sensitivity, and the instrument function of the spectrometers used to record the spectra is not adequately known, further limiting the usefulness of these data.
(4) Deviations from Lambert–Beer's law have been reported [24], indicating unresolved spectral structures in existing glyoxal spectra.
(5) The differential cross-section, which is the basis for the DOAS measurements, is currently not well known.

Overall, an improved knowledge of the UV–vis spectrum of glyoxal is required for the DOAS applications.

While the IR spectrum of glyoxal has been the subject of numerous studies, including line-by-line analysis [31,32], no near simultaneous measurements in the UV–vis and IR spectral regions are yet available. The latter are required to provide a common calibration standard independent of spectral region, thereby facilitating the direct comparison of DOAS, Fourier transform infrared (FTIR), tunable diode laser (TDL), and cavity ring down spectroscopic (CRD) measurements of glyoxal in laboratory and field applications.

In this study, the same mixtures of glyoxal in nitrogen were recorded sequentially in the UV–vis and IR at high spectral resolution in the same apparatus. The study had the following five objectives:

(1) To improve the spectral calibration of the glyoxal absorption cross-sections.
(2) To explain previously observed deviations from Lambert–Beer's law.
(3) To reduce the uncertainty in the calculation of photolysis frequencies (*J*-values) of glyoxal.
(4) To compare and cross calibrate UV–vis and IR spectral features.
(5) To provide a UV–vis spectrum of sufficient resolution to enable calculation of glyoxal reference spectra for DOAS applications.

2. Experimental

Light-absorption by gas molecules is described by Lambert–Beer's law. After traversing a distance L in the presence of an absorber of concentration C, the intensity $I_0(\lambda)$ (in the absence of any absorber) is reduced to $I(\lambda)$ according to:

$$I(\lambda) = I_0(\lambda)\mathrm{e}^{-\sigma CL}$$

The negative exponent is referred to as optical density, and CL is the column density of the absorber. The absorption cross-section σ was calculated from the following equation:

$$\sigma = \frac{\ln I_0(\lambda)/I(\lambda)}{CL}$$

Absorption spectra of glyoxal were recorded using the high-resolution Fourier-transform spectrometer (Bruker IFS-120 HR) at the University of Bremen. The spectrometer has been described in detail elsewhere [33]. The Fourier transform spectrometer (FTS) was combined with a commercial Bruker A 134 long path absorption gas cell as is shown in Fig. 1. The absorption cell is mounted vertically on the measurement chamber of the FTS. Its overall constructive length and volume are ∼83.5 cm and ∼15,000 cm^3, respectively. The gas cell is made of glass with stainless steel flanges at both ends. Through the lower flange, the analysis light is transferred from the FTS into the cell and out of the cell towards the FTS' detector chamber. At the upper flange, the gas inlet, the connector for the pressure sensors and a port for evacuation are located. The gas inlet consists of two tubes to simultaneously fill the vessel at the top and the bottom for improved homogeneity. This gas cell contains a White type multi reflection optical arrangement, which enables optical path lengths of 1.64 m to about 40 m. The measurements were conducted at the minimum pathlength of 1.64 m, which required some adjustment of the mirror system after the cell to assure proper illumination of the detector. The mirrors are aluminum coated, without further protective coating. The pressure in the absorption cell was measured using three temperature stabilized capacitive pressure transducers of 1 Torr, 10 Torr and 1000 mbar range (MKS Baratron), and yielded a high linearity and reproducibility of the

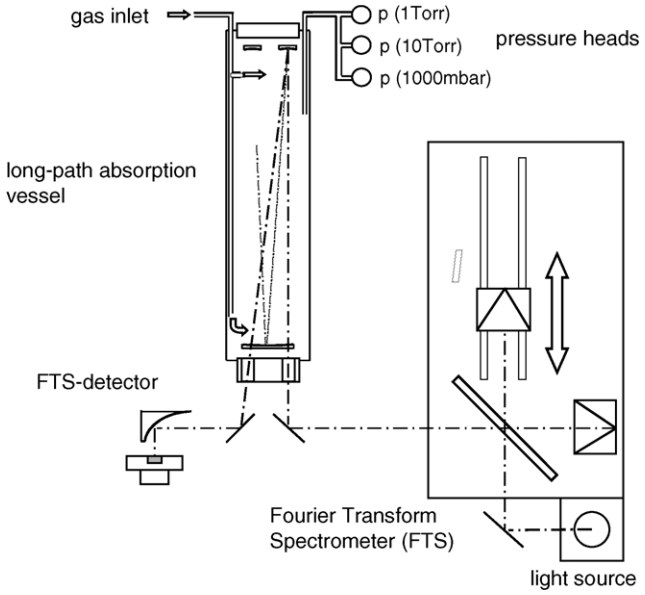

Fig. 1. A schematic diagram of the measurement set-up. Measurement light passed through the evacuated FTS and traversed the multi-pass cell twice before it was focussed onto the detector for recording of the interferogram. A 15 l cell was used to reduce wall effects, and light-exposure of only a small portion of this volume reduced glyoxal photolysis. The pressure was measured using three capacitance manometers of different ranges.

pressure reading (10^{-4} error ≡ 0.0001 Torr for the 1 Torr sensor ≡ 0.00013 mbar). A water-cooled Xenon arc lamp (Osram XBO 150W/2) with an elliptical mirror (Amko) was used as source of UV and vis light, and a globar lamp was the source of IR radiation. The various combinations of beam-splitters and detectors together with the unapodized spectral resolution used to derive the datasets are listed in Table 1. The interferometer chamber was evacuated to about 0.03 mbar during the experiments, primarily to eliminate water bands from the IR spectra. Wavenumbers and wavelengths in this paper have been calculated for 1 atm of air.

The experimental configuration of the FTS is summarized in Table 1; five different datasets designated as I through V were recorded. The final UV–vis absorption cross-section was derived from the datasets Ib, IIIa and IIIb in 1 atm of N_2 (see Table 1). All measurements were made at a temperature of 296 ± 1 K. Under these conditions the Doppler width of transitions near 400 nm is ∼0.04 cm^{-1} and the full width at half maximum (FWHM) arising from pressure and Doppler broadening is ∼0.14 cm^{-1} (∼0.1 cm^{-1} in the infrared), neglecting pre-dissociation. The ^1A_u electronic state of glyoxal is predissociative, and spectral features will indeed be broader. The unapodized spectral resolution (boxcar) was selected as 0.06 cm^{-1} to resolve the pressure broadened spectral features at wavelengths larger 368 nm. Towards shorter wavelength, the spectral resolution was set 1 cm^{-1}. Test spectra recorded at higher spectral resolution indicated that this is at least three times finer than the effective widths of glyoxal features in this wavelength range. Datasets IIIa and IIIb were recorded to maximize signal-to-noise of low cross-section values, while avoiding saturation of the strong transitions. The main source of uncertainty in the recording of UV spectra has been identified as drifts in the lamp output in spectral regions where the lamp signal is comparatively small (see Fig. 1 in [33], $\nu > 30000\ cm^{-1}$). To overcome this problem two sets of low-resolution measurements were recorded (datasets Ia and II), which reduced the time between acquisition of spectra recorded in the presence and absence of glyoxal to being of the order of 10 min. Individual baseline spectra were interpolated from sample spectra of the empty cell recorded before and after addition of glyoxal. The integrated cross-sections extracted from six different glyoxal fillings in dataset Ia yielded agreement within 0.5–3% (see Table 2 for average values). These integral cross-sections were used to scale a UV-spectrum taken at higher spectral resolution and substantially longer acquisition times (dataset Ib). Corrections for lamp-drifts were calculated as the difference in the integral cross-section derived from datasets

Table 1
Experimental set-up and conditions

Dataset	Experimental configuration	Gas cell pressure	Objective for the analysis[a]
Ia	D: UV-diode, BS: QuarzIII, Res: 20 cm^{-1}	2–13 mbar glyoxal	Scale dataset Ib, correct baseline drift
Ib	Res: 1 cm^{-1}	ca. 5.6 mbar glyoxal in 1 atm of N_2	40000–27147cm^{-1} (250–368 nm)
II	D: Gap/InSb-diode, BS: CaF_2, Res: 4/0.2 cm^{-1}	0.01–0.1 mbar glyoxal	Intercalibration of spectral ranges, Scale datasets IIIa, IIIb and IV
IIIa	D: GaP-diode, BS: QuarzIII, Res: 0.06 cm^{-1}	ca. 0.4 mbar glyoxal in 1 atm N_2	cross-section >7 × 10^{-20} cm^2, 25137.07–25136.38 cm^{-1} (397.8 nm), 24887.02–24736.99 cm^{-1} (401.8–404.3 nm), 24324.86–21889.90 cm^{-1} (411.1-456.8 nm)
IIIb		ca. 13.4 mbar glyoxal in 1 atm N_2	cross-section <7 × 10^{-20} cm^2, 27147–25137.07 cm^{-1} (368–397.7 nm), 25136.38–24887.02 cm^{-1} (397.8–401.8 nm), 24736.99–24324.86 cm^{-1} (404.3–411.1 nm), 21889.90–19005.30 cm^{-1} (456.8–526.2 nm)
IV	D: MCT, BS: CaF_2, Res: 1 cm^{-1}	ca. 0.16 mbar glyoxal in 1 atm N_2	Integral cross-sections for IR
V	D: InSb-diode, BS: CaF_2, Res: 0.009 cm^{-1}	0.2–1 mbar glyoxal in 1–1013 mbar of N_2	Pressure effect on sigma IR

Abbreviations: D: detector; BS: beam-splitter; Res: spectral resolution.
[a] Wavenumbers in 1 atm N_2.

Table 2
UV–vis and IR absorption cross-sections of glyoxal at 296 K

Dataset		Absolute cross-section		Integrated cross-section	
		Position[a]	(cm^2 $molecule^{-1}$)	Region[a]	(cm $molecule^{-1}$)
Ia	UV spectrum			39098–38901	$(3.36 \pm 0.11) \times 10^{-19}$
				37009–36992	$(4.50 \pm 0.11) \times 10^{-19}$
				34012–33989	$(8.62 \pm 0.03) \times 10^{-19}$
				31010–30992	$(3.12 \pm 0.04) \times 10^{-19}$
		28499	$(3.8 \pm 0.2) \times 10^{-21}$	28528–28467	$(2.32 \pm 0.07) \times 10^{-19}$
Ib		39000	$(16.5 \pm 2.5) \times 10^{-21}$		
		37000	$(25.6 \pm 0.7) \times 10^{-21}$		
		34000	$(36.9 \pm 0.2) \times 10^{-21}$		
		31000	$(18.1 \pm 0.2) \times 10^{-21}$		
		28571	$(3.8 \pm 0.2) \times 10^{-21}$		
II	Intercalibration of UV and IR range			22288–21836	$(71.0 \pm 3.5) \times 10^{-18}$[b]
				2724–2940	$(16.5 \pm 0.8) \times 10^{-18}$[b]
IIIa	UV–vis spectrum	22719.99	$(105.1 \pm 5.4) \times 10^{-20}$		
IIIb		27092.68	$(1.36 \pm 0.07) \times 10^{-20}$		
		19203.66	$(4.96 \pm 0.25) \times 10^{-20}$		
IV	IR spectrum	4584	$(1.68 \pm 0.15) \times 10^{-20}$	4662–4456	$(7.8 \pm 0.7) \times 10^{-19}$
		3461	$(3.89 \pm 0.25) \times 10^{-20}$	3512–3402	$(10.8 \pm 0.7) \times 10^{-19}$
		2847	$(35.0 \pm 1.8) \times 10^{-20}$	2724–2940	$(16.5 \pm 0.8) \times 10^{-18}$
		1740	$(81.5 \pm 4.1) \times 10^{-20}$	1807–1643	$(22.7 \pm 1.1) \times 10^{-18}$
V	IR @ 0.2 mbar glyoxal	2820.460	$(276 \pm 14) \times 10^{-20}$		
	IR @ 100 mbar N_2	2820.455	$(141 \pm 7) \times 10^{-20}$		
	IR @ 300 mbar N_2	2820.465	$(82.7 \pm 4.1) \times 10^{-20}$		
	IR @ 1013 mbar N_2	2820.470	$(46.3 \pm 2.3) \times 10^{-20}$		

[a] Units: wavenumbers in 1 atm of air.
[b] Integral over the differential cross-section.

Ia and Ib, interpolated linearly between the center points of the intervals of dataset Ia (see Table 2). Similarly, spectra of dataset III were baseline corrected by assuming negligible absorption at 19,000 cm^{-1}, a sigma of 3.8×10^{-21} cm^2 at 28,499 cm^{-1} (determined from dataset Ia), and in between linear interpolation of baseline drifts. The baseline drift corrected spectra of dataset III were scaled to match the integral differential cross-section of dataset II. An overview of the magnitude of these corrections and other potential error sources is given in Table 3.The relation between integral absorption cross-sections (dataset II in Table 2) and glyoxal pressure was linear to within 1% for pure glyoxal pressures between 0.013–0.11 mbar (vis) and 0.013–0.27 mbar (IR). Leakage of ambient air into the cell was generally small ($\tau_{leak} \approx 6 \times 10^{-6}$ $mbar\,s^{-1}$) but found to limit the measurement accuracy of small glyoxal pressures. It was therefore decided to monitor the pressure increase before and after glyoxal addition for several minutes and extrapolate the observed cell leak rate to the time of glyoxal addition as shown in Fig. 2, in order to more precisely determine the amount of added glyoxal. Use of only two traverses in the gas cell minimized glyoxal absorption while maximizing signal-to-noise. Overall the experimental approach taken enabled low glyoxal pressures (0.013 mbar, see Fig. 2) to be determined at a precision which was not limited by the accuracy of the pressure measurement. Accounting for the small leak rate yielded systematically higher cross-section values and the correction of 4% in Table 3 corresponds to the magnitude of this effect over 100 s (a typical time to fill the cell).

Glyoxal is removed from the White cell as a result of photolysis in the measurement light, deposition to the walls, and OH-radical reactions (via HO_2-radical formation after glyoxal photolysis in UV-light, their recombination and subsequent photolysis of H_2O_2). These effects were minimized by the choice of a large-volume White cell, where only a small fraction of the White cell volume was exposed to measure-

Table 3
Characterization of potential error sources

Potential error source	Maximum correction (%)	Error (after correction) (%)
Baseline drift (>30000 cm^{-1})	16.4	0.5–3.0
Baseline drift (<30000 cm^{-1})	5.4	≤1
Leakage into gas cell	4.0	≤0.5
Photolysis in measurement light	1.8	≤0.2
Wall deposition	1.0	≤0.1
Pressure measurement		≤1.5
Interpolation method		2.0
Pathlength		0.5
Reproducibility of synthesis		0.2
Purity of synthesis		≤1
Polymerization		≤0.5
Leakage during glyoxal transfer		≤0.1
Overall error UV		<5
Overall error vis and IR		<3

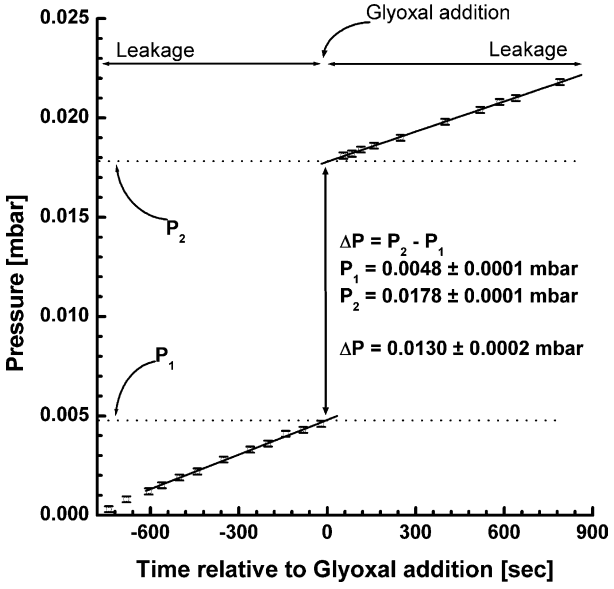

Fig. 2. Illustration of the procedure to determine the amount of glyoxal added to the gas cell. For low glyoxal pressures, the leak rate of ambient air, although small, becomes a limiting source of error. This leak rate was characterized (here $\tau_{leak} = 5.4 \times 10^{-6}$ mbar s^{-1}) and the glyoxal partial pressure is derived as the difference in pressures before and after glyoxal addition, extrapolated to the time of glyoxal addition.

ment light. In an attempt to minimize HO_2-radical formation, a nearly oxygen free buffer gas was used (ppm levels in N_2). Photochemical loss (photolysis and OH-reaction) and wall-deposition of glyoxal were reduced by keeping acquisition times short (dataset II), and losses were characterized in separate experiments to be $\tau_{phot} = 5.5 \times 10^{-6}$ s^{-1} (UVIII beam splitter) and $\tau_{wall} = 2.6 \times 10^{-6}$ s^{-1}. The added amount of glyoxal was corrected for photochemical loss and wall deposition, taking into account the residence time of glyoxal in the gas cell, and exposure times to UV- or IR-light. The reduced acquisition time in recording datasets Ia and II is reflected in small corrections of up to a few percent (see Table 3). The error of scaling datasets Ib and III from the integral absorption cross-sections was assessed by recording test spectra at different resolution and comparing integral differential cross-sections in the vis spectral range (near 22,000 cm^{-1}). Use of the differential absorption cross-section eliminates any baseline drifts and this quantity was found to be reproducible and independent of the spectral resolution to within 2%. This number was taken to account for the effect of spectral resolution on the base-points used by the OPUS software to determine integral absorptions. Dataset IIIb was used to check for the formation of any formaldehyde within the cell; no indications for such contamination were observed.

The comparison and cross calibration of the absorption spectra in the UV–vis and IR spectral ranges was undertaken by using dataset II. The chosen set-up (see Table 1) enabled the same glyoxal filling to be observed quasi-simultaneously in the vis and IR spectral ranges. Two sets of IR absorption cross-sections were recorded. Dataset IV provides a low-resolution measurement with an unapodized spectral resolution of 1 cm^{-1}, typical of that needed for FTIR applications. In addition, high-resolution spectra, dataset V, were recorded at an unapodized spectral resolution of 0.009 cm^{-1} and a variety of pressures (see Tables 1 and 2).

Glyoxal was prepared by heating equal masses of glyoxal trimeric dihydrate and P_2O_5 (both Aldrich) to 423 K. The gas-phase was continuously pumped via a trap immersed in an ethanol-bath kept at 173 K. Glyoxal was collected as yellow crystals, and further purified by trap-to-trap distillation to ice/water temperature. Pure gas-phase glyoxal was stored in a 10 l bulb at pressures not exceeding 15 mbar, and typically used directly after preparation. Any air leakage during glyoxal transfer was controlled, and influenced the glyoxal partial pressure in the bulb to <0.1%. FTIR spectra with high concentrations of glyoxal added to the gas cell revealed no indication for CO and CO_2 impurities. A similar procedure to that used in this study has been claimed to yield glyoxal with >99% purity [24]. No significant difference in the cross-sections was observed for different synthesis batches. Even after several days of storage, glyoxal cross-sections determined in the vis spectral range (near 22,000 cm^{-1}) were reproducible within 0.2%. This implies that formation of polymers did not affect our pressure calibration (see Table 3).

The combination of all error sources yields an overall error, which is somewhat dependent on the spectral range (see Table 3). In all spectral ranges the uncertainty in the cross-section is 5% or better, but not less than 2×10^{-22} cm^2 mol^{-1}.

3. Result and discussion

3.1. Comparison with literature data

The UV–vis absorption cross-sections of glyoxal obtained in this and other studies are shown in Fig. 3, and a more detailed comparison is compiled in Table 4. Agreement is generally good in the unstructured part of the spectrum (UV-region) where the cross-section proves less sensitive to the effect of spectral resolution (see Table 4). In spectral regions where overlap exists, including the structured part of the spectrum, the agreement is especially good between our spectrum and the ones determined by teams from the Max Planck Institute (MPI) [24] and the National Center for Atmospheric Research (NCAR) [23]. However, our value is about 10% higher and this difference appears to be significant within the low experimental uncertainties of this work. Interestingly, the sum of the changes, which account for photochemical loss of glyoxal, wall-deposition and leakage, results in an upward correction in the final cross-section (up to 7%, see Table 3), which is comparable to the difference of our value with those from these previous studies. Deviations near 350 nm are considerably larger with other investigations [15,22]. These differences are attributed to the higher relative uncertainty of the

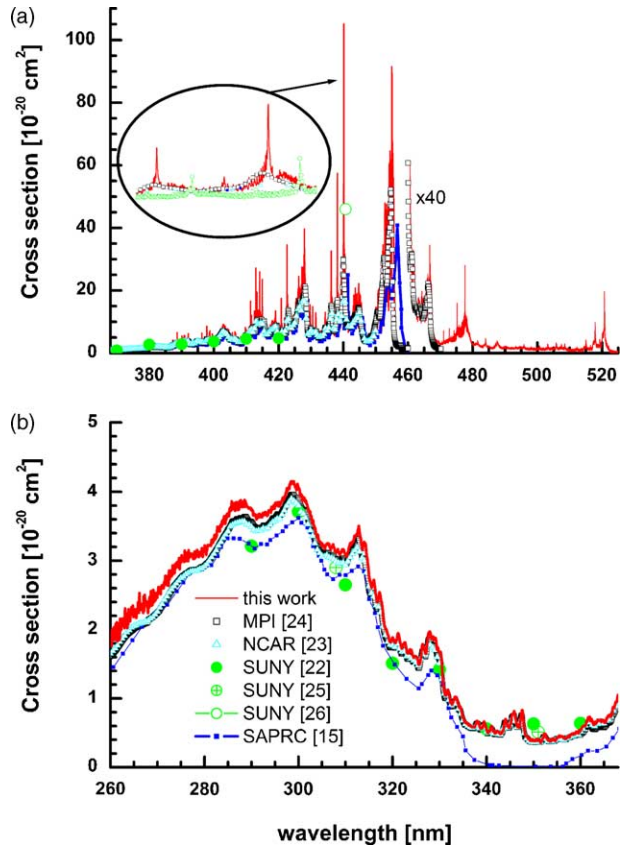

Fig. 3. The UV–vis absorption cross-section spectrum of glyoxal from this work compared to the data from MPI [24], NCAR [23], SUNY [22,25,26] and SAPRC [15]; (a) the visible region of the spectrum; in the inset the region from 438.8 to 441 nm has been expanded; values above 460 nm have been multiplied by 40 (b) the UV region of the spectrum.

low cross-section values, and possibly a somewhat uncertain wavelength calibration (see Table 4).

The scatter among available data becomes considerably larger in the highly structured part of the spectrum ($\lambda > 368$ nm). The difference in spectral resolution needs to be accounted for to allow for a meaningful comparison among spectra. The high-resolution spectrum from this work was therefore convoluted using a Gaussian-shape line-function of variable width to match the spectral resolution of other work prior to any comparison. Further, for each spectrum two quantities were characterized (Table 4):

(1) The integral cross-section was calculated over the wavelength range from 431 to 460 nm (431–450 nm for [23], 436–442 nm for [26]), and is given as the ratio to the integrated value of this work in Table 4 (denoted "integral σ-ratio").
(2) The differential cross-section was compared using least-squares fitting, where the resolution adjusted data from this work was used to model the spectra from other work. Fitting was carried out in the above wavelength ranges, applying a linear shift and a fifth order polynomial as a high-pass filter; results are given in Table 4 (denoted "fit coefficient").

From comparison of the columns "integral σ-ratio" and "fit coefficient", it is possible to assess each spectrum in terms of apparent deviations from Lambert–Beer's law, which arise when spectral features are not fully resolved by the instrument. Indeed, such deviations appear to affect all previous work. This tends to be less visible in the work undertaken at higher spectral resolution [24,26,30] as would be expected. In the MPI work [24], such deviations were investigated near 455 nm, where at low spectral resolution the strongest absorp-

Table 4
Comparison with available literature values

Reference	Spectral resolution[a]	UV-region (350 nm) (10^{-20} cm^2)	Vis-region (440 nm) (10^{-20} cm^2)	Integral σ-ratio (rel units)	Fit coefficient[c] (rel units)	shift[c] (nm)
UV–vis spectral ranges						
This work	~0.001		105	1.00	1.00	
	0.01		98			
	0.1	0.38/0.41[b]	53			
	1.0	0.39	26			
SUNY [22]	0.01	0.63				
SUNY [25]	0.01	0.51				
SUNY [26]	0.01		46	0.48	0.44	0.56
EUPHORE [30]	0.17		33	0.89	0.86	0.10
MPI [24]	0.25	0.36	30	0.94	0.87	0.39
NCAR [23]	0.6	0.36	17	0.93	0.69	-0.03
SAPRC [15]	n.n.	0.01	25	0.83	0.64	1.08
IR spectral range						
NCAR [23]	1 cm^{-1}			1.05		
NIES [44]	1 cm^{-1}			0.80		
FORD [34]	0.25 cm^{-1}			0.98		
BUGH [45]	1 cm^{-1}			0.74		

[a] FWHM value in nm, unless noted otherwise.
[b] Notation: $\sigma_{350\,nm}/\sigma_{351\,nm}$. For ref. [25] sigma at 351 nm needs be compared.
[c] Least squares fit, after adjusting for resolution (see Section 3.1).

Table 5
Absorption cross-section[a] σ (10^{-20} cm^2/molecule) of glyoxal at 296 K

λ (nm)	σ	λ (nm)	σ	λ (nm)	σ	λ (nm)	σ	λ (nm)	σ
250	1.725	306	3.223	362	0.706	418	7.873	474	0.108
251	1.520	307	3.200	363	0.639	419	9.134	475	0.159
252	1.477	308	3.146	364	0.680	420	5.602	476	0.155
253	1.545	309	3.123	365	0.665	421	7.188	477	0.181
254	1.596	310	3.100	366	0.743	422	6.990	478	0.255
255	1.667	311	3.222	367	0.860	423	13.045	479	0.142
256	1.619	312	3.343	368	1.012	424	8.239	480	0.074
257	1.809	313	3.390	369	1.063	425	10.448	481	0.070
258	1.823	314	3.233	370	1.139	426	16.411	482	0.065
259	1.850	315	2.805	371	1.185	427	16.101	483	0.053
260	1.828	316	2.646	372	1.141	428	21.424	484	0.071
261	1.957	317	2.460	373	1.212	429	6.499	485	0.050
262	2.027	318	2.214	374	1.352	430	7.027	486	0.041
263	2.144	319	1.927	375	1.332	431	6.518	487	0.056
264	2.184	320	1.854	376	1.377	432	6.082	488	0.070
265	2.261	321	1.885	377	1.467	433	5.657	489	0.042
266	2.333	322	1.766	378	1.605	434	6.809	490	0.045
267	2.371	323	1.723	379	1.534	435	7.660	491	0.041
268	2.361	324	1.677	380	1.934	436	13.187	492	0.039
269	2.475	325	1.603	381	2.455	437	9.185	493	0.040
270	2.509	326	1.606	382	2.019	438	13.822	494	0.041
271	2.613	327	1.695	383	2.069	439	12.135	495	0.042
272	2.720	328	1.937	384	1.939	440	25.942	496	0.045
273	2.810	329	1.857	385	1.893	441	13.118	497	0.033
274	2.920	330	1.689	386	1.835	442	9.013	498	0.035
275	3.000	331	1.128	387	2.287	443	11.124	499	0.032
276	3.060	332	1.048	388	3.000	444	13.460	500	0.033
277	3.087	333	0.966	389	3.206	445	15.110	501	0.038
278	3.078	334	0.919	390	3.483	446	7.818	502	0.031
279	3.086	335	0.737	391	3.922	447	3.730	503	0.042
280	3.135	336	0.630	392	3.801	448	4.144	504	0.034
281	3.216	337	0.589	393	2.852	449	5.527	505	0.035
282	3.322	338	0.647	394	3.147	450	8.682	506	0.046
283	3.455	339	0.585	395	3.855	451	13.817	507	0.042
284	3.568	340	0.553	396	3.679	452	15.945	508	0.037
285	3.673	341	0.563	397	3.361	453	30.368	509	0.030
286	3.797	342	0.510	398	4.323	454	26.902	510	0.023
287	3.791	343	0.499	399	4.345	455	51.990	511	0.023
288	3.813	344	0.649	400	3.873	456	15.666	512	0.030
289	3.800	345	0.624	401	4.455	457	2.661	513	0.023
290	3.734	346	0.733	402	5.843	458	2.201	514	0.030
291	3.643	347	0.631	403	7.159	459	0.902	515	0.053
292	3.654	348	0.604	404	6.237	460	1.202	516	0.035
293	3.681	349	0.415	405	4.491	461	0.883	517	0.051
294	3.729	350	0.391	406	4.482	462	0.588	518	0.102
295	3.809	351	0.395	407	4.066	463	0.322	519	0.065
296	3.824	352	0.423	408	3.444	464	0.339	520	0.100
297	3.922	353	0.415	409	4.008	465	0.330	521	0.169
298	4.073	354	0.403	410	5.661	466	0.416	522	0.037
299	4.123	355	0.422	411	7.221	467	0.522	523	0.011
300	4.045	356	0.443	412	7.406	468	0.149	524	0.007
301	3.905	357	0.431	413	10.753	469	0.091	525	0.004
302	3.779	358	0.471	414	10.115	470	0.076	526	0.000
303	3.567	359	0.503	415	10.194	471	0.086		
304	3.350	360	0.546	416	6.073	472	0.092		
305	3.242	361	0.627	417	6.829	473	0.110		

[a] Averaged over 1 nm intervals, and given for the central wavelength of each interval.

tion band appears (see Table 5); a linear increase of absorption with glyoxal partial pressure was indeed observed. However, from our high resolution work, the strongest absorption peak is revealed at a different wavelength, i.e. near 440 nm, requiring the linearity of the Lambert–Beer's law to be checked at this wavelength.

In the IR spectral range the scatter among the integral absorption cross-sections is about 25%. Agreement is within few percent with the work from NCAR [23] and Ford Motor Company (FORD) [34]. It is noteworthy that spectra recorded at larger column densities tend to show smaller integral cross-section values.

Comparing the spectral or wavelength calibration of our spectra with previous work yields good agreement with the studies from NCAR [23] and the European Photo Reactor (EUPHORE) [30]. A significant shift was observed in the spectrum determined at the State University of New York (SUNY) [26] (see the inset of Fig. 3a). The overall wavenumber accuracy of our FTS is inferred to be $\leq 0.05\,cm^{-1}$, by recording NO_2 absorptions and comparing them to cross-sections calibrated from I_2 calibrations [33].

3.2. Linear range of Lambert–Beer's law in UV–vis and IR

In the UV–vis spectral range, deviations from Lambert–Beer's law have been reported in ref. [24]. It was concluded, however, that these deviations have an insignificant effect on the absorbance of glyoxal at the peak absorption near 455 nm at column densities below 10^{18} mol/cm^2. The effect of column density on the apparent low-resolution absorption was modelled from our data in Fig. 4. Deviations from linearity are indeed strongest near 440 nm, where at high-resolution the absorption cross-section is found to peak. Distortions in the apparent shape of the low-resolution spectrum become visible at even lower column densities (few 10^{17} mol/cm^2). It is demonstrated here that the deviations from Lambert–Beer's law are caused by the considerable ro-vibronic structure, which, when observed at low spectral resolution, results in the apparent absorption to become dependent on the column density of glyoxal.

Provided the absorption is adequately resolved, then a constant relationship between the absorber concentration and its optical density is obtained, and Lambert–Beer's law holds. In practise, the optical density for which Lambert–Beer's law remains linear is a function of the apparatus and the observed trace gas. The term 'non-linearity' in the behaviour of the optical density with respect to the Lambert–Beer's law is defined here as the optical density of a spectrum that results in a residual of more than one per thousand, i.e. 0.1% (typical noise-level), when scaled linearly and subtracted from any spectrum of smaller optical density. Following this definition, the vis spectrum of glyoxal was shown to obey Lambert–Beer's law up to an optical density of 10% at 440 and 0.25 nm spectral resolution. Any spectra recorded at larger optical densities

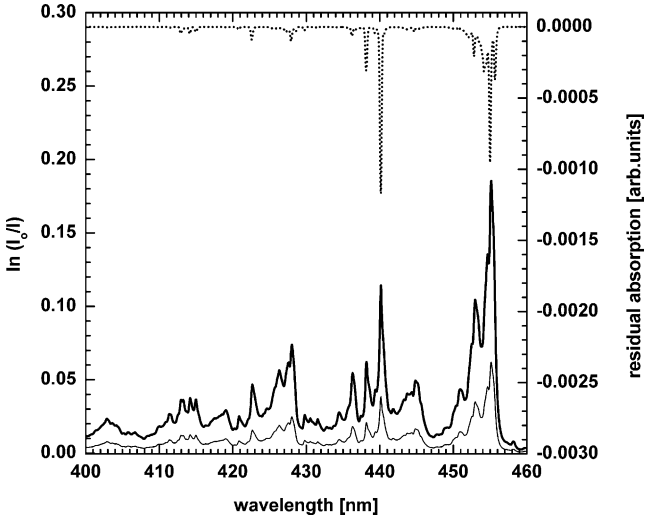

Fig. 4. Modeling the deviations from Lambert–Beer's law reported in ref [24]. Two high-resolution spectra corresponding to column-densities of 10^{17} mol/cm^2 (thin line) and 3×10^{17} mol/cm^2 (thick line) were convoluted to 0.25 nm spectral resolution (FWHM); (dotted line) residual structure after the two spectra were scaled to match in column-density and subtracted. This distortion of the spectrum can be understood from its ro-vibronic structure, which—when observed at low spectral resolution—causes the apparent absorption cross-section to depend on the column density of glyoxal.

do not obey Lambert–Beer's law, and alternative approaches [35] need to be employed to avoid non-linear absorptions to cause residual structures during spectra evaluation.

Similarly, the linear range of the IR band system near $2835\,cm^{-1}$ extends to an optical density of 9% at a spectral resolution of $1\,cm^{-1}$ (see Fig. 5). In Fig. 6 panel (b), the spectra from dataset V are shown to illustrate the effect of

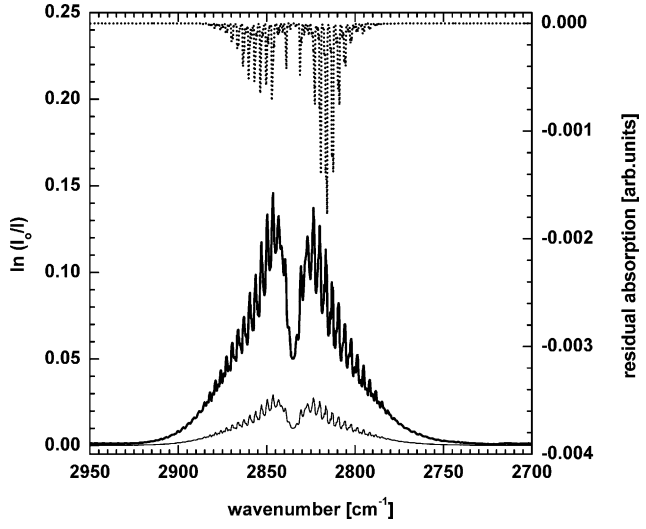

Fig. 5. Deviations from Lambert–Beer's law in the IR spectral range are illustrated for the asymmetric C–H-stretch transition near $2847\,cm^{-1}$. Two high-resolution spectra corresponding to column-densities of 8.7×10^{16} mol/cm^2 (thin line) and 4.3×10^{17} mol/cm^2 (thick line) were convoluted to $1\,cm^{-1}$ spectral resolution (FWHM); (dotted line) residual structure after the two spectra were scaled to match in column-densities and subtracted. For explanations see Section 3.2.

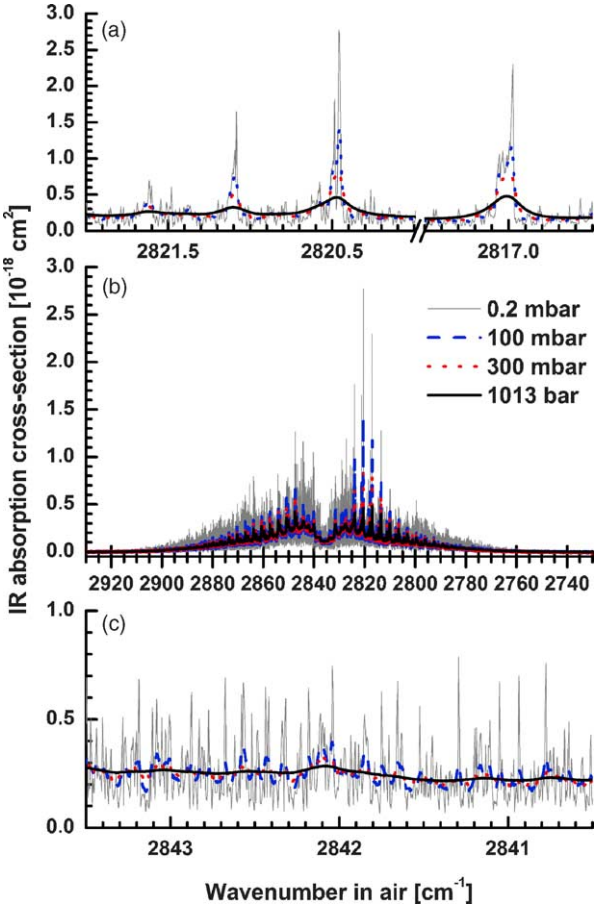

Fig. 6. The effect of pressure broadening in the IR spectrum. Panel (b) shows the spectra recorded under the conditions of dataset V. Panel (a) shows two expansions of the spectrum where rotational–vibrational structure remains visible up to 1 bar total pressure. Panel (c) shows a part of the spectrum (note change in scales), where the rich rotational-vibrational structure at low pressures is traded for a rather continuous absorption formed by overlapping pressure-broadened line wings at 1 bar total pressure, see Section 3.2 for details.

pressure broadening by nitrogen on the IR spectrum. Panel (a) shows two expansions of spectral regions, where a structured portion of the cross-section remains visible on top of a continuous (unstructured) absorption formed from overlapping Voigt-wings of the pressure broadened lines at 1 bar total pressure. The FWHM of the structured portion is $\geq 0.2\,cm^{-1}$ (envelope of several lines), in approximate agreement with typical pressure broadening of $\sim 0.1\,cm^{-1}$ (FWHM) per atmosphere. At 1 bar total pressure the rotational-vibrational structure in the spectra of dataset V can hence be regarded fully resolved. Panel (c) shows another part of the spectrum, where the rich rotational-vibrational structures at low pressures is almost completely lost (at 1 bar total pressure) and an apparently near constant absorption cross-section results (note change in scale). For the band near 1740 cm^{-1}, considerable rotational-vibrational structure is known to exist at low pressures [32]. The effect of pressure broadening, however, is not well established. At 1 bar of nitrogen and at 1 cm^{-1} spectral resolution the P-, Q- and R-branches are visible as a rather unstructured envelope absorption. Deviations from Lambert–Beer's law were observed at even lower optical densities than at 2835 cm^{-1}, suggesting that some spectral structure exists at 1 bar total pressure (similar to panel (a) in Fig. 6).

3.3. Calculation of photolysis frequencies

The UV–vis absorption cross-section of glyoxal is needed for calculations of the photolysis frequency (J-value) of glyoxal in the atmosphere. Glyoxal J-values as a function of wavelength were calculated using our cross-section spectrum, and quantum yields from ref. [36]. The UV-photon actinic flux was calculated for different solar zenith angles (SZA) from the TUV model [37] for a standard atmosphere, cloudless sky and a surface albedo of 10% (typical for urban environments). The results are shown in the upper panel of Fig. 7 as a function of wavelength; the integral over wavelength corresponding to $J_{CHOCHO} = 1.15 \times 10^{-4}\,s^{-1}$. As is apparent, more than 80% of glyoxal photolysis takes place at wavelengths shorter than 370 nm. In the lower panel of Fig. 7, the uncertainty in absorption cross-section of glyoxal is assessed with respect to its impact on the uncertainty in the calculated J-value. Taking the variability among available literature values as the uncertainty in sigma (dotted line), the integral over the uncertainty in glyoxal photolysis (meshed gray shaded area) corresponds to about 40% of the overall J-value. About 60% of this uncertainty is constrained to a narrow wavelength interval between 330 and 375 nm, where the low value of the absorption cross-section has a considerably larger relative uncertainty associated to it. The uncertainty in the absorption cross-section of glyoxal from ref. [24] (thin line) and this work (thick line) show a similar spectral distribution, but the error of this work is considerably smaller. The uncertainty in the J-values based on the uncertainty in the absorption cross-section from this work is about half that of ref. [24] and corresponds to about 6% (three-sigma confidence level).

The J-value and photolytic lifetime of glyoxal are plotted as a function of SZA in Fig. 8. Our cross-section values result in a J-value, which is slightly but significantly higher than calculations based on [24]. Error bars correspond to the three-sigma confidence level, and account for the error in sigma only. Both J-values are in general agreement with measured photolysis rates of glyoxal in the presence of natural sunlight, which are typically $1.0 \times 10^{-4}\,s^{-1} \pm 0.15 \times 10^{-4}\,s^{-1}$ (SZA $\sim$ 20–30°) [16,36]. The approximately 10% difference in J-values can easily be accounted for in terms of the uncertainty in quantum yields. Photolysis quantum yields are currently not well established and will briefly be discussed.

The dependence of absolute quantum yields on total pressure was previously investigated using two sets of broad-band light-sources that emit light at wavelengths below and above $\sim$370 nm, respectively, TL/12 and TL/3 lamps [36,38]. At shorter wavelength (TL/12 lamps overlap with the diffuse $\tilde{B} - \tilde{X}$ band, see Fig. 9 in [36]) the quantum yields were found to be independent of pressure and $\phi_{TL/12\text{-}MPI} = 0.97 \pm 0.03$

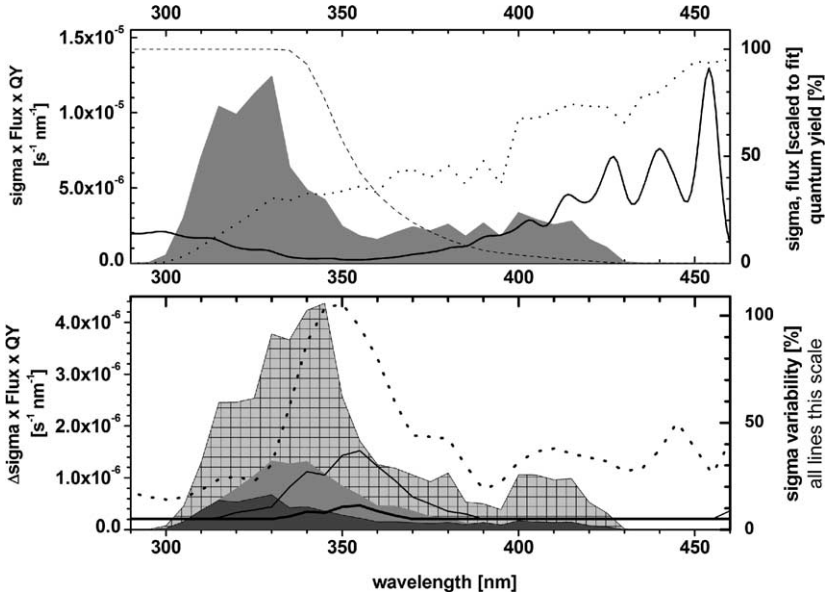

Fig. 7. Glyoxal photolysis frequencies (*J*-values) as a function of wavelength (SZA = 10°). Upper panel: (solid line) low resolution cross-section of glyoxal, (dotted line) relative profile of the UV-photon actinic flux, (dashed line) photolysis quantum yield from ref. [36], all right scale; (shaded gray) d*J*/dλ, left scale. Lower panel: uncertainty of sigma taken as (dotted line) the variability among all literature data, (thin line) ref. [24], (thick line) this work, all lines right scale; uncertainty in d*J*/dλ due to uncertainty in sigma for (meshed light gray) variability among all literature data, (shaded gray) ref. [24], (shaded dark gray) this work, all left scale.

(average for values determined at 100–700 Torr). This value was based on the MPI cross-section, and is well below unity, i.e. $\phi_{\text{TL/12-IUP}} = 0.91 \pm 0.03$, if calculated with the cross-section from this study. This is in good agreement with quantum yields shown in Fig. 7 (taken from Table 16 of ref. [36]), which drop below unity already at wavelength >335 nm. At wavelengths >370 nm TL/3 lamps overlap with the structured

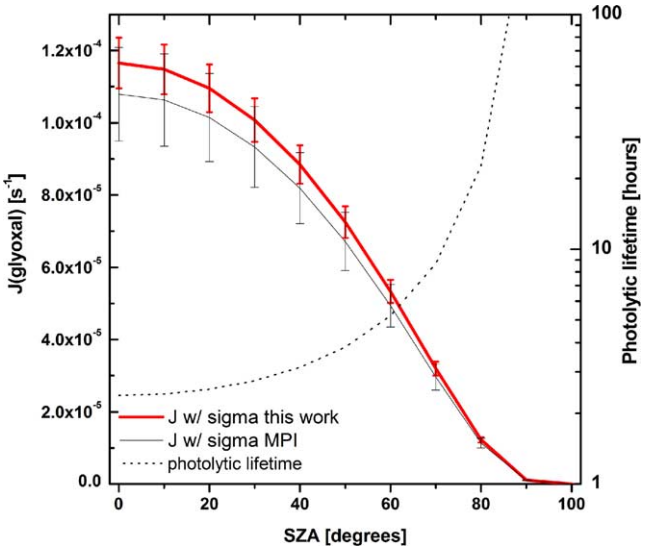

Fig. 8. *J*-values and photolytic lifetime of glyoxal in the atmosphere. Calculations of two *J*-values use the cross-section determined in this work (thick line), and of ref. [24] (thin line). Error bars indicate the uncertainty due to the cross-section only (3-sigma confidence level); (dashed line) lifetime of glyoxal with respect to photolysis, see Section 3.3 for details.

$\tilde{A}\ ^1A_u - \tilde{X}\ ^1A_g$ band (see Fig. 9 in [36]). The quantum yields determined for TL/3 lamps were found to decrease with pressure to values of $\phi_{\text{TL/3-MPI}} = 0.043 \pm 0.002$ at 700 Torr, corresponding to $\phi_{\text{TL/3-IUP}} = 0.040 \pm 0.002$ based on this work.

A more recent study employed laser flash-photolysis to determine wavelength dependent quantum yields of HCO radicals [22]. The pressure dependence of the quantum yields was confirmed. In the pressure dependent region, i.e. λ > 370 nm, the quantum yields decreased with increasing pressure, and some indications for a pressure dependence were observed already at shorter wavelengths. This behavior was attributed to the competition between decomposition and collisional quenching of excited glyoxal. From their data, the lower limit for the pressure dependent quantum yield for glyoxal to yield two HCO-radicals corresponds to $\phi_{\text{2HCO}} \geq 0.07$ (420 nm and 760 Torr). The existence of additional photolysis channels at shorter wavelengths would only increase the overall quantum yields at 760 Torr. TL/3 lamps have maximum light output around 420 nm, and the difference in the pressure dependent quantum yields [22,36,38] is significant. Ab initio calculations rationalize experimentally observed photolysis channels from ground state glyoxal [39–42]; little theoretical information is as yet available on the role of excited states [22,43] under atmospheric conditions. Using the higher quantum yields [22] in calculations of *J*-values results in the overestimation of experimental values by about a factor of two [16,36]. From our high-resolution cross-section data it is interesting to note that ro-vibronic structure in the spectrum is observed at wavelength larger than 368 nm, while essentially no such structure is observed towards shorter wavelengths. Especially with use of narrow-band light sources (bandwidth

~0.01 nm in ref. [22]) extrapolations of quantum yields to atmospheric pressure need to adequately take into account the effect of pressure on the mean cross-section value over the laser bandwidth. Our high-resolution cross-section provides a means to investigate this matter further. The main uncertainty in *J*-value calculations is currently associated with the pressure dependent quantum yields towards longer wavelengths, which appear to be at the lower edge of available literature values. In addition, the wavelength at which the overall quantum yield drops below unity is not well established.

The "effective" quantum yield ϕ_{eff} is defined as the average quantum yield over the entire absorption region at wavelengths longer than 295 nm, calculated as the ratio of the measured *J*-value under natural sunlight conditions to the calculated *J*-value using unit quantum yield. Based on the MPI spectrum it was determined $\phi_{\text{eff-MPI}} = 0.038 \pm 0.01$ for conditions relevant for the troposphere [18,36]. The ratio of the integral cross-section between 295 and 526 nm from this work to ref. [24] is 0.925, and $\phi_{\text{eff-IUP}} = 0.035 \pm 0.01$ based on this work. Within the about 25% uncertainty of measured *J*-values these values are indistinguishable.

3.4. Implications for mechanism development of aromatic hydrocarbons

The branching ratio for glyoxal formation has been determined from a variety of aromatic hydrocarbons using DOAS for the detection of glyoxal [2,30]. The uncertainty in sigma (then estimated at 20%) accounted for about half of the overall uncertainty in the yields. Re-evaluated on the basis of the cross-section from this work, glyoxal yields from the reaction of OH-radicals with benzene, toluene and *p*-xylene ($32.0 \pm 5\%$), ($30.6 \pm 6\%$), and ($31.9 \pm 5\%$), respectively. These values are lower than those published earlier [2], and about 50% improved in error. The conclusions on a negligible secondary yield of glyoxal remain unchanged.

4. Conclusions

High-resolution measurements of the UV–vis absorption cross-section of glyoxal are reported between 250 and 526 nm. The wavelength range of the spectrum is extended and its wavelength calibration is improved. Cross-section values are found to be about 10–30% higher than the most recent low-resolution work.

The origin of the deviation from Lambert–Beer's law behaviour of the absorption features, observed in the MPI work [24], is explained by the rich ro-vibronic structure in the visible part of the spectrum. The peak absorption cross-section is found near 440 nm, about 15 nm blue shifted from the maximum seen at low spectral resolution. Simulations of the column-density dependence of the low-resolution cross-section indicate this region to be most sensitive with respect to deviations from Lambert–Beer's law, and explain part of the scatter among existing literature values. Further potential explanations for the differences may lie in the careful calibration of the pressure measurement undertaken in this study, and the attempts to minimize and account for leaks, photochemical losses induced from the measurement light, and the deposition of glyoxal at the wall.

The UV–vis spectrum enables glyoxal reference spectra to be calculated for DOAS applications in the atmosphere. Further, it allows an improved calculation of glyoxal photolysis frequencies, as the uncertainty of low cross-section values near 350 nm has been reduced by a factor of eight (to now ~5%). The ro-vibronic structure observed at wavelength above 368 nm indicates that pressure broadening of the cross-section should be taken into account when interpreting quantum yields determined with narrow-band light sources. The dominant uncertainty with determining *J*-values is currently associated with the pressure dependent quantum yields at longer wavelengths, which appear on the lower edge of the available literature data, and the wavelength dependence of quantum yields.

Re-evaluation of the glyoxal yields from [2] on the basis of this work lead to slightly smaller glyoxal yields, which are about 50% reduced in error. Our near simultaneous measurements of the UV–vis and IR absorption cross-sections provide a database for the comparison and validation of measurements of glyoxal made using different spectroscopic techniques: DOAS, Fourier transform infrared interferometry (FTIR), tunable diode lasers (TDL) and cavity ring-down spectroscopy (CRD).

Acknowledgements

We thank Heike Kromminga for her helpful comments and assistance. This work was carried out with financial contributions from the European Union project IALSI, the German Aerospace Agency (DLR), the German Ministry for Education and Research (BMBF), and the University of Bremen. This study is a contribution to the objectives of the EU ACCENT Network of excellence, and the IGBP IGAC and SOLAS projects.

References

[1] J.G. Calvert, R. Atkinson, K.H. Becker, R.H. Kamens, J.H. Seinfeld, T.J. Wallington, G. Yarwood, The Mechanisms of Atmospheric Oxidation of Aromatic Hydrocarbons, Oxford University Press, Oxford, 2002.
[2] R. Volkamer, U. Platt, K. Wirtz, J. Phys. Chem. A 105 (2001) 7865.
[3] H. Bandow, N. Washida, Bull. Chem. Soc. Jpn. 58 (1985) 2549.
[4] D.F. Smith, T.E. Kleindienst, C.D. Mciver, J. Atm. Chem. 34 (1999) 339.
[5] D. Grosjean, Environ. Sci. Technol. 24 (1990) 1428.
[6] R.I. Martinez, J.T. Herron, J. Phys. Chem. 92 (1988) 4644.
[7] X.Y. Liu, H.E. Jeffries, K.G. Sexton, Atm. Environ. 33 (1999) 3005.
[8] S. Hatakeyama, N. Washida, H. Akimoto, J. Phys. Chem. 90 (1986) 173.
[9] I. Magneron, R. Thevenet, A. Mellouki, G. Le Bras, G.K. Moortgat, K. Wirtz, J. Phys. Chem. A 106 (2002) 2526.

[10] E. Grosjean, D. Grosjean, J. Atm. Chem. 32 (1999) 205.
[11] A.J. Kean, E. Grosjean, D. Grosjean, R.A. Harley, Environ. Sci. Technol. 35 (2001) 4198.
[12] D. Grosjean, E. Grosjean, A.W. Gertler, Environ. Sci. Technol. 35 (2001) 45.
[13] M. Yamaguchi, J. Ishida, X.X. Zhu, M. Nakamura, T. Yoshitake, J. Liquid Chromatogr. 17 (1994) 203.
[14] A. Barros, J.A. Rodrigues, P.J. Almeida, M.T. Oliva-Teles, J. Liquid Chromatogr. Relat. Technol. 22 (1999) 2061.
[15] C.N. Plum, E. Sanhueza, R. Atkinson, W.P.L. Carter, J.N. Pitts, Environ. Sci. Technol. 17 (1983) 479.
[16] B. Klotz, F. Graedler, S. Sorensen, I. Barnes, K.H. Becker, Int. J. Chem. Kinet. 33 (2001) 9.
[17] S. Matsunaga, K. Kawamura, Anal. Chem. 72 (2000) 4742.
[18] G.K. Moortgat, Pure Appl. Chem. 73 (2001) 487.
[19] E. Grosjean, D. Grosjean, M.P. Fraser, G.R. Cass, Environ. Sci. Technol. 30 (1996) 2687.
[20] G.K. Moortgat, D. Grossmann, A. Boddenberg, G. Dallmann, A.P. Ligon, W.V. Turner, S. Gab, F. Slemr, W. Wieprecht, K. Acker, M. Kibler, S. Schlomski, K. Bachmann, J. Atm. Chem. 42 (2002) 443.
[21] E. Grosjean, P.G. Green, D. Grosjean, Anal. Chem. 71 (1999) 1851.
[22] Y.Q. Chen, L. Zhu, J. Phys. Chem. A 107 (2003) 4643.
[23] J.J. Orlando, G.S. Tyndall, Int. J. Chem. Kinet. 33 (2001) 149.
[24] A. Horowitz, R. Meller, G.K. Moortgat, J. Photochem. Photobiol. A-Chem. 146 (2001) 19.
[25] L. Zhu, D. Kellis, C.F. Ding, Chem. Phys. Lett. 257 (1996) 487.
[26] L. Zhu, G. Johnston, J. Phys. Chem. 99 (1995) 15114.
[27] G. Herzberg, Molecular Spectra and Molecular Structure, R.E. Krieger Pub. Co, Malabar, Fla, 1989.
[28] D.A. Ramsay, M. Vervloet, F. Vanhorenbeke, M. Godefroid, M. Herman, J. Mol. Spectrosc. 149 (1991) 348.
[29] D.A. Ramsay, C. Zauli, Acta Phys. Acad. Sci. Hungar. 35 (1974) 79.
[30] R. Volkamer, A DOAS study on the oxidation mechanism of aromatic hydrocarbons under simulated atmospheric conditions, Dissertation, University of Heidelberg, Germany, 2001, http://archiv.ub.uni-heidelberg.de/volltextserver/volltexte/2002/1939/.
[31] A.R.H. Cole, G.A. Osborne, J. Mol. Spectrosc. 36 (1970) 376.
[32] R.W. Larsen, F. Hegelund, J. Ceponkus, B. Nelander, J. Mol. Spectrosc. 211 (2002) 127.
[33] S. Voigt, J. Orphal, J.P. Burrows, J. Photochem. Photobiol. A-Chem. 149 (2002) 1.
[34] H. Niki, P.D. Maker, C.M. Savage, L.P. Breitenbach, Int. J. Chem. Kinet. 17 (1985) 547.
[35] R. Volkamer, T. Etzkorn, A. Geyer, U. Platt, Atm. Environ. 32 (1998) 3731.
[36] G.K. Moortgat (Ed.), RADICAL: Evaluation of Radical Sources in Atmospheric Chemistry Through Chamber and Laboratory Studies, ENV4-CT97-0419, JRC Ispra, Italy, 2001, for copies moo@mpch-mainz.mpg.de.
[37] S. Madronich, S. Flocke, The Role of Solar Radiation in Atmospheric Chemistry, Springer, Berlin, 1998.
[38] J. Tadic, G.K. Moortgat, 2004, personal communication.
[39] X.S. Li, J.M. Millam, H.B. Schlegel, J. Chem. Phys. 115 (2001) 6907.
[40] X.S. Li, J.M. Millam, H.B. Schlegel, J. Chem. Phys. 114 (2001) 8897.
[41] X.S. Li, H.B. Schlegel, J. Chem. Phys. 114 (2001) 8.
[42] D.M. Koch, N.H. Khieu, G.H. Peslherbe, J. Phys. Chem. A 105 (2001) 3598.
[43] C.C. Kao, M.L. Ho, M.W. Chen, S.J. Lee, I.C. Chen, J. Chem. Phys. 120 (2004) 5087.
[44] B. Klotz, 2001, personal communication.
[45] A. Bierbach, Produktuntersuchungen und Kinetik der OH-initiierten Gasphaswnoxidation aromatischer Kohlenwasserstoffe sowie ausgew ahlter carbonylisher Folgeprodukte, BUGH Wuppertal, Germany, 1994.